Generation of quadratic spatially trapped beams with short pulsed light

F Baronio[1]**, A Barthélémy**[2]**, S Carrasco**[3]**, V Couderc**[2]**,
C De Angelis**[1]**, L Lefort**[2]**, Y Min**[4]**, P H Pioger**[2]**, V Quiring**[4]**,
L Torner**[3] **and W Sohler**[4]

[1] Istituto Nazionale per la Fisica della Materia, Università di Brescia, via Branze 38,
25123 Brescia, Italy
[2] Faculté des Sciences, Institut de Recherches en Communications Optiques et Microondes,
123 Avenue A Thomas, 87060 Limoges, France
[3] ICFO—Institut de Ciències Fotòniques, and Department of Signal Theory and
Communications, Universitat Politechnica de Catalunya, Barcelona, ES 08034, Spain
[4] Angewandte Physik, Universität Paderborn, 33095 Paderborn, Germany

Abstract
We report a numerical and experimental investigation on the generation of
spatial self-narrowed beams with short temporal pulsed excitation in
quadratic film waveguides. The impact of temporal group-velocity
mismatch between the quadratic multiple interacting signals is shown. We
accurately studied the spatial, temporal and spectral signals dynamics versus
pulse power and phase mismatch. We show that spatial self-trapping can be
induced even if the pump pulse duration is significantly shorter than the
group delay mismatch between interacting waves for large enough positive
phase mismatches.

Keywords: nonlinear optics, quadratic soliton, cascading, harmonic
generation

(Some figures in this article are in colour only in the electronic version)

1. Introduction

Cascaded $\chi^{(2)}$:$\chi^{(2)}$ parametric interactions of high intensity
light beams in materials with quadratic nonlinearities offer a
rich variety of phenomena [1]. In particular, they can yield
strong nonlinear refraction effects at relatively low power
levels. Thus second-order cascading processes have gained
relevance similar to that of their third-order counterparts for
use in switching devices that rely on large optically induced
nonlinear phase changes. Even though this subject has been
investigated since the early 1970s [2], only recently has it
been revisited and applied to all-optical signal processing
with the purpose of overcoming the limits of $\chi^{(3)}$ materials
(see [3–6] and references therein). Interest in this field has
been maintained by the fascinating range of new phenomena
encountered and their potential applications, such as soliton
propagation, all-optical switching and logic for ultrafast signal
processing devices.

Multicolour spatial soliton formation mediated by the
cascading of quadratic nonlinearities has been demonstrated
experimentally in a variety of geometries (see [7–13] and
references therein). In this case spatial solitons are formed
by the mutual trapping of the waves parametrically interacting
in the nonlinear medium. Solitons exist in particular in
the process of second-harmonic generation (SHG) that is
addressed here (see [11, 13] for reviews and [12–18] for
the properties and excitation conditions of the simplest
families), where multidimensional soliton families exist above
a threshold light intensity for all values of the phase mismatch
between the fundamental frequency (FF) and the second-
harmonic (SH) waves.

Spatial solitons are non-diffracting, self-trapped beams
formed with continuous-wave light signals. However, in
practice potential applications of the self-trapped beams to
ultrafast photonic devices require picosecond excitation. With
such short pulses one might expect serious difficulties in

the generation of a multicolour spatially self-trapped beam near phase matching, due to the temporal group velocity mismatch (GVM) between FF and SH waves and to their strong interaction and mutual dragging near phase matching [19, 20]. The minimum pulse width is of paramount relevance as it will give the limit of the processing speed of the envisaged all-optical devices.

In this paper, we report a numerical and experimental investigation on the generation of spatial self-trapped beams with picosecond temporal pulsed excitation in periodically poled Ti-in-diffused lithium niobate (Ti:PPLN) slab waveguides, with only the FF wave at 1548 nm in input. The impact of temporal GVM on the evolution of quadratically interacting waves is described in this paper. We accurately studied the spatial, temporal and spectral signals dynamics versus pulse power and phase mismatch. We show that spatial self-narrowing can be induced for large positive phase mismatch and above a threshold intensity even if the pump pulse duration is shorter than the group delay mismatch between interacting FF and SH waves. We show temporal GVM compensation in a spatial self-trapped regime. Temporal and spectral behaviours that accompany spatial trapped propagation are highlighted.

2. Experimental set-up

The experiments were performed with a 58 mm long (L) and 10 mm wide planar waveguide fabricated in a z-cut LiNbO$_3$ substrate by in-diffusion of a 70 nm thick, vacuum-deposited Ti layer at 1060 °C. An uniform micro-domain structure of periodicity $\Lambda = 16.9$ μm (duty cycle 0.5) has been generated after waveguide fabrication by electric-field-assisted poling. The sample was inserted in a temperature stabilized oven to allow operation at elevated temperatures ($T = 110–180$ °C); in this way, photorefractive effects ('optical damage') could be minimized. Moreover, temperature tuning of the phase-matching conditions in the PPLN region became possible. An all-fibre laser system was used as the source of 4 ps pulses (FWHM in intensity) at 1548 nm (FF) with a peak power of a few kilowatts at 20 MHz repetition rate.

The spectral bandwidth of the input beam is 1.7 nm which represents 5.3 times the spectral acceptance bandwidth of the PPLN. The thickness of the waveguide permits the propagation of a single TM$_0$ mode of 4 μm width at the FF; several TM modes are supported at the SH, but only the TM$_0$ of 3 μm width is efficiently pumped by the TM$_0$ at the FF. The laser beam was shaped in a highly elliptical spot, nearly Gaussian in profile, with a FWHM in intensity of 76 μm along the non-guided dimension and 3.9 μm along the perpendicular direction. The beam was polarized parallel to the z axis of the PPLN for access to the material's largest quadratic nonlinear coefficient $\chi^{(2)}_{zzz} = 54$ pm V^{-1} ($2d_{33}$). The spatial beam profiles were recorded by scanning a magnified image of the pattern with a photodiode. Temporal characterizations were monitored by a background-free non-collinear auto-correlator and by a background-free non-collinear cross-correlator.

3. Numerical model

We model the electric fields E_1 and E_2 at ω_0 (FF) and $2\omega_0$ (SH), respectively, with $\omega_0 = 2\pi/\lambda_0$ and $\lambda_0 = 1548$ nm free space

wavelength, propagating in the y direction, as

$$
\begin{aligned}
E_1(x, y, z, t) &= \tfrac{1}{2}[m_1(z)a_1(x, y, t) \\
&\quad \times \exp(-\mathrm{j}(\beta_{\omega_0} y + \omega_0 t)) + \text{c.c.}] \\
E_2(x, y, z, t) &= \tfrac{1}{2}[m_2(z)a_2(x, y, t) \\
&\quad \times \exp(-\mathrm{j}(\beta_{2\omega_0} y + 2\omega_0 t)) + \text{c.c.}]
\end{aligned}
\tag{1}
$$

where $m_1(z)$ and $m_2(z)$ are the mode profiles in the guided dimension, $a_1(x, y, t)$ and $a_2(x, y, t)$ are the slowly varying envelopes, that obey the nonlinear coupled equations [1]:

$$
\begin{aligned}
&\mathrm{j}\frac{\partial a_1}{\partial y} - \mathrm{j}\beta'_{\omega_0}\frac{\partial a_1}{\partial t} - \frac{\beta''_{\omega_0}}{2}\frac{\partial^2 a_1}{\partial t^2} + \frac{1}{2\beta_{\omega_0}}\frac{\partial^2 a_1}{\partial x^2} \\
&\quad + \frac{\chi^{(2)}\omega_0}{2cn_{\omega_0}}\frac{\int m_2|m_1|^2\,\mathrm{d}z}{\int |m_1|^2\,\mathrm{d}z}a_2 a_1^* e^{-\mathrm{j}\Delta ky} = 0 \\
&\mathrm{j}\frac{\partial a_2}{\partial y} - \mathrm{j}\beta'_{2\omega_0}\frac{\partial a_2}{\partial t} - \frac{\beta''_{2\omega_0}}{2}\frac{\partial^2 a_2}{\partial t^2} + \frac{1}{2\beta_{2\omega_0}}\frac{\partial^2 a_2}{\partial x^2} \\
&\quad + \frac{\chi^{(2)}\omega_0}{2cn_{2\omega_0}}\frac{\int m_2|m_1|^2\,\mathrm{d}z}{\int |m_2|^2\,\mathrm{d}z}a_1^2 e^{\mathrm{j}\Delta ky} = 0
\end{aligned}
\tag{2}
$$

where β represents the propagation constant, β' is the group velocity, β'' is the inverse group-velocity dispersion, n is the refractive index, $\Delta k = 2\beta_{\omega 0} - \beta_{2\omega 0} + K_S$ is the effective mismatch, where $K_S = 2\pi/\Lambda$ and $\chi^{(2)} = 2/\pi\chi^{(2)}_{zzz}$ is the nonlinear coefficient.

To model the pulse propagation, two different numerical tools have been used. A standard finite difference vectorial mode solver was employed to determine the linear propagation properties in the slab waveguide, i.e. the mode profiles, the effective index, the propagation constant, the inverse group velocity and the inverse group velocity dispersion [21–23]. In the case at hand the crystal length corresponds to 3.2 times the FF diffraction length and up to 4.8 times the walk-off length between FF and SH; the dispersive terms can be neglected. The phase-mismatch temperature dependence corresponds approximately to 1π °C^{-1}. Finally, using a finite difference beam propagation technique, we solved the nonlinear coupled equations (equations (2)).

4. Spatial characterization

Experiments and numerical simulations were carried out varying the input pulse power and phase-mismatch conditions via the temperature of the sample, keeping fixed the temporal and spatial widths of the FF injected pulse. First we measured the spatial profiles of the FF output beam, along the free propagation direction versus the injected intensity at different phase mismatches. Regardless of the phase-mismatch conditions, at the low intensity regime, the FF beam broadened because of diffraction inside the crystal. In the quasi-linear regime the output beam profile had a width $w_{ox} = 246$ μm which corresponds to the diffracted input beam ($w_{ox} = 76$ μm) after 58 mm of propagation along the waveguide (figure 1). At large enough phase-mismatch values ($\Delta kL > 9\pi$), at the high-intensity regime, the nonlinear self-focusing effect balances the effect of diffraction, thus causing the formation of a spatially FF self-narrowed beam (figure 2). Typical dependences of the output spatial profile width on the injected intensity, at different fixed positive phase-mismatch conditions, are reported in figure 3. In the
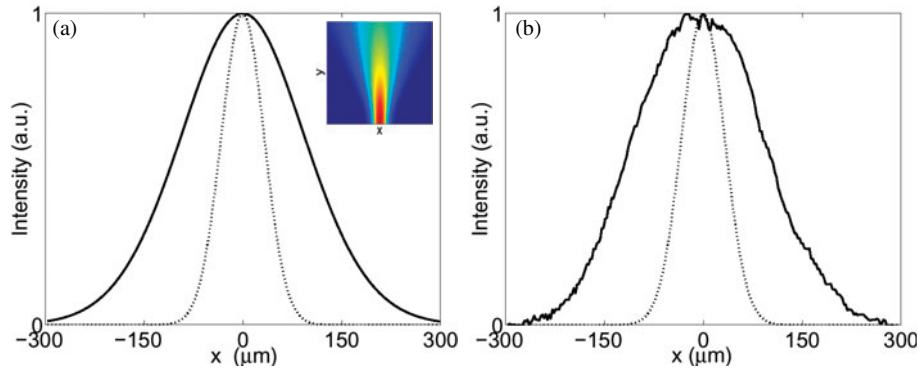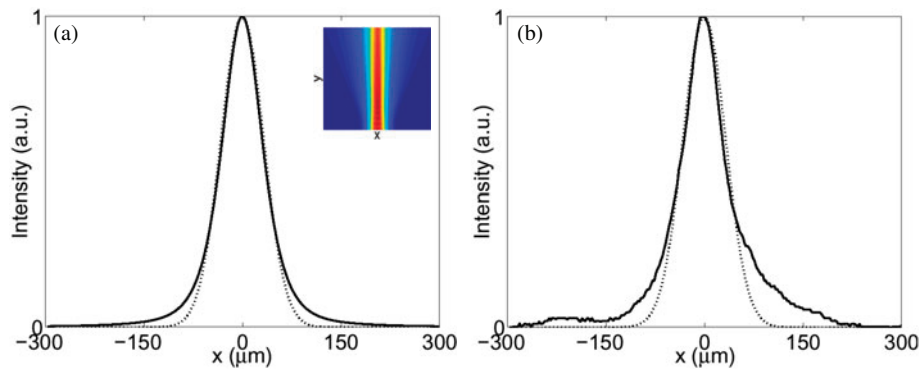
Figure 1. Spatial profile of the FF beam, integrated in time, at the input (dotted curve) and output (full curve) in the quasi-linear regime. (a) Numerical simulations and (b) experimental data. The inset shows the numerical FF beam evolution in the (x, y) plane. Here the phase mismatch is $\Delta kL = 18\pi$ ($T = 142\,°C$) and the input intensity is $I = 1$ MW cm^{-2}.
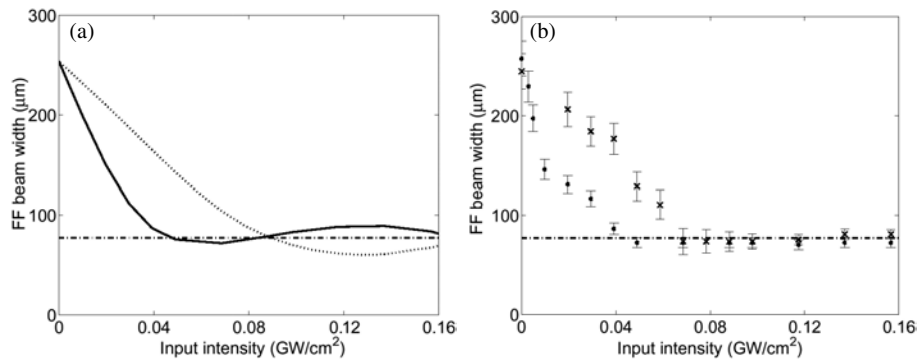

Figure 2. Spatial profile of the FF beam, integrated in time, at the input (dotted curve) and output (full curve) in the nonlinear self-trapped regime. (a) Numerical simulations and (b) experimental data. The inset shows the numerical FF beam evolution in the (x, y) plane. Here the phase mismatch is $\Delta kL = 18\pi$ ($T = 142\,°C$) and the input intensity is $I = 66$ MW cm^{-2}.

Figure 3. FWHM in intensity of the output FF beam versus injected input intensity for different phase-mismatch conditions (or temperatures). (a) Numerical simulations: full curve, $\Delta kL = 9\pi$; dotted curve, $\Delta kL = 30\pi$; chain curve, input width. (b) Experimental data: circles, $T = 151\,°C$ ($\Delta kL = 9\pi$); crosses, $T = 130\,°C$ ($\Delta kL = 30\pi$); chain curve, input width.

limit of the available power (590 W), it was not possible to observe self-focusing effects at negative phase-mismatch values and in close vicinity of perfect phase-matching $\Delta kL = 0$ ($T = 160\,°C$). Spatial trapping started to appear at a sample temperature of $151°$ C ($\Delta kL \sim 9\pi$) and was maintained, with a linear increase of the intensity threshold, down to $T = 114\,°C$ ($\Delta kL \sim 46\pi$). This trend is illustrated in figure 4 and is consistent with the fact that, in the limit of large Δk, the effective Kerr nonlinearity is proportional to Δk^{-1}. Thus, at such limit the intensity needed to compensate the diffraction scales linearly with the wavevector mismatch.

It is clearly demonstrated that self-narrowed beams have been generated at large mismatch despite temporal walk-off and short-pulse excitation. Thus group-velocity mismatch can prevent spatial trapping at negative phase mismatch and near phase matching, but trapping does occur at a large enough positive phase mismatch, in full agreement with the predictions reported in [19].

5. Temporal characterization

The temporal behaviours of the signals have also been analysed. In the experiments temporal characterizations were
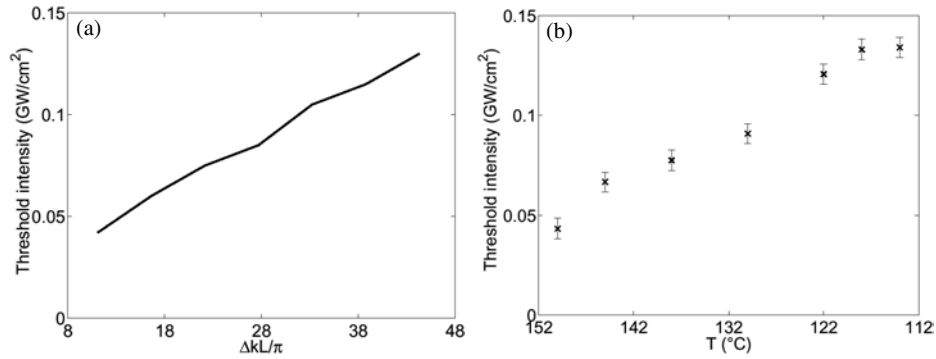
Figure 4. Input FF intensity threshold for the generation of self-trapped beams versus phase mismatch (temperature). (a) Numerical simulations, (b) experimental data.
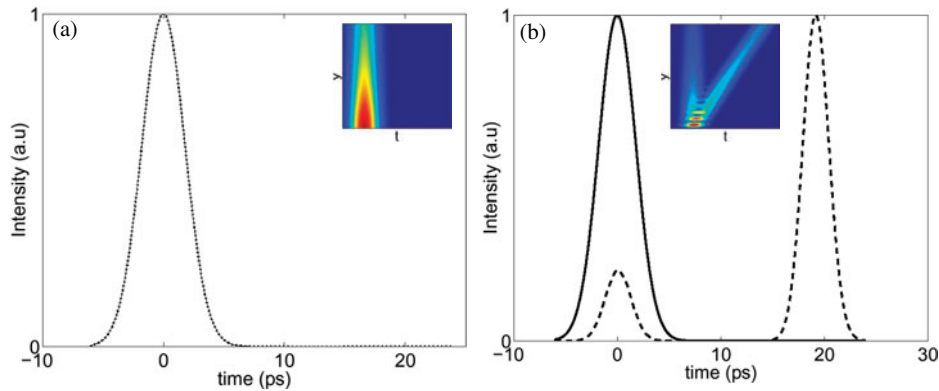

Figure 5. Quasi-linear regime. (a) Calculated FF pulse profiles at the input (dotted curve) and output (full curve). (b) Calculated FF (full curve) and SH (broken curve) pulses at output. The temporal slices of the signals are for $x = 0$. The insets show the numerical FF (a) and SH (b) temporal evolution in the (t, y) plane. Here the phase mismatch is $\Delta k L = 18\pi$ ($T = 142\,°\text{C}$) and the input intensity is $I = 1$ MW cm^{-2}.

monitored by a background-free SHG non-collinear auto-correlator. A cross-correlator technique was also used to provide information on the relative temporal distributions of the signals. The cross-correlation measurement is based on a background-free auto-correlator. Both the pulses at the FF and the SH are launched on the two arms of the correlator; a BBO crystal is oriented for non-collinear sum frequency generation of the FF and SH waves; a spatial filter and a colour glass filter select the sum frequency wave before detection.

In particular we focused on the temporal characterization of pulses versus the injected intensity at positive phase mismatches, i.e. under conditions where spatial self-narrowing is achievable. In the low-intensity regime, when the nonlinear effect does not balance the FF spatial diffraction, we note that the calculated FF and SH output pulses do not overlap in time and do not lock together (figure 5); the FF and SH pulses generated in the early stage of propagation behave quasi-linearly, experience different group velocities and do not remain temporally overlapped. Only a small contribution at the SH overlap in time. This property has also been revealed experimentally during the measurement of cross-correlation traces between the pulses at FF and at SH. In figure 6 we show typical experimental and numerical cross-correlation traces at output, for the same input intensity and phase mismatch of figure 5. The main outer peaks testify the existence of a strong contribution at SH separated from the FF wave by 20 ps on the temporal axis. This time delay corresponds to the delay experienced by a SH pulse, generated in the

early stage of the FF wave propagation, that walks off from the FF pulse because of the linear GVM. The 20 ps delay corresponds to the temporal walk off ($\delta_t \sim 3.3$ ps cm^{-1}) accumulated after 58 mm of propagation along the waveguide. The central contribution in the cross-correlation traces denotes that a small part at the SH remains almost overlapped in time with the FF pulse. The calculated output FF temporal intensity envelope does not reveal any distortion or modulation at the intensity regime displayed (figure 5). Significant distortions were observed in the simulations at higher input intensities. In figure 7 we compare the intensities of the measured and simulated autocorrelation traces of the FF at input and output.

Typical FF and SH output temporal envelopes, in the high-intensity regime, when the nonlinear focusing effect balances the FF spatial diffraction, are reported in figure 8. In figure 9 we show experimental and numerical cross-correlation traces at output, for the same input intensity and phase mismatch of figure 8. Despite a strong walk-off, the output pulse at the FF and a consistent contribution at the SH overlap in time and lock together, thus providing an appreciable self-focusing effect by cascading. Only a small part of the SH pulse undergoes the GVM influence completely. At positive phase mismatch and in the high-intensity regime a nonlinear compensation of the temporal GVM became possible. The temporal GVM compensation, and thus the temporal overlapping between the two beams, is a crucial condition for an effective focusing cascading interaction. The simulations of the experimental conditions show that the FF output pulses exhibit a small
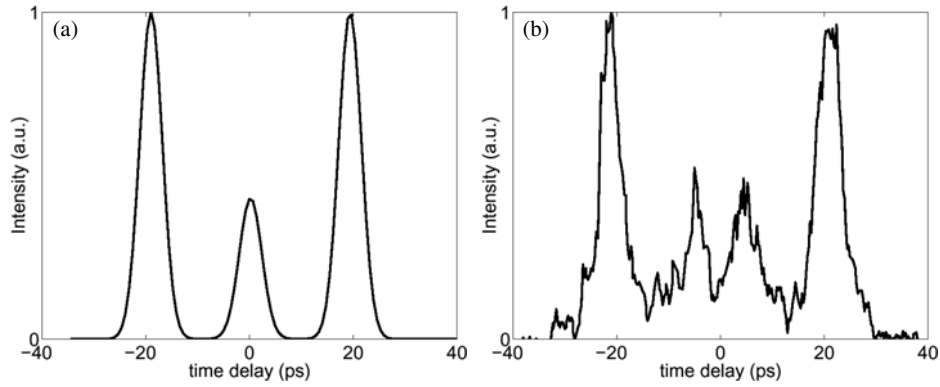
Figure 6. Quasi-linear regime. Cross-correlation trace in intensity of the FF and SH signals at output. (a) Numerical simulation, (b) experimental data. Here the phase mismatch is $\Delta kL = 18\pi$ ($T = 142\,°C$) and the input intensity is $I = 1\ \mathrm{MW\ cm^{-2}}$.
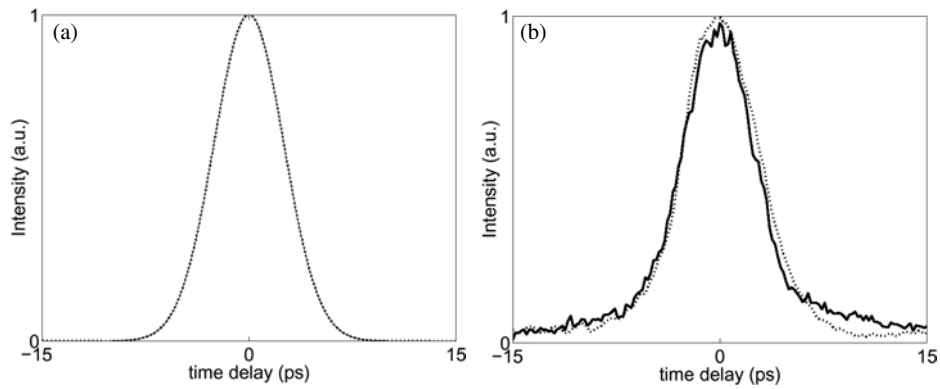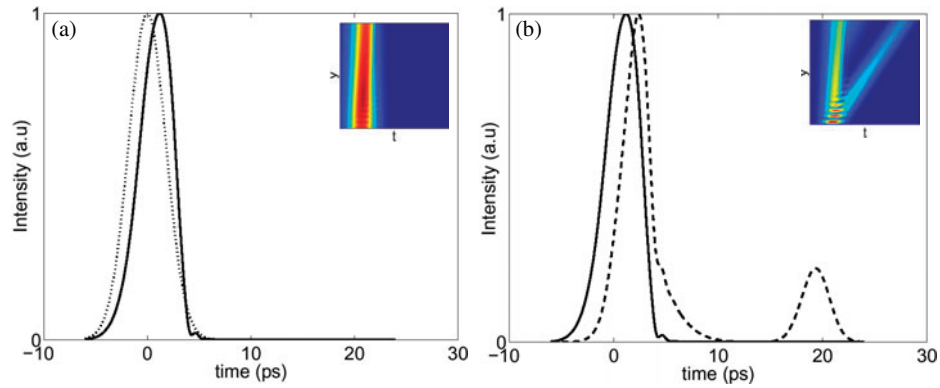

Figure 7. Quasi-linear regime. Autocorrelation traces in intensity of the FF at the input (dotted curve) and output (full curve). (a) Numerical simulation, (b) experimental data. Here $\Delta kL = 18\pi$ ($T = 142\,°C$) and the input intensity is $I = 1\ \mathrm{MW\ cm^{-2}}$.

Figure 8. Spatial self-trapped regime. (a) Calculated FF pulse profiles at the input (dotted curve) and output (full curve). (b) Calculated FF (full curve) and SH (broken curve) pulses at output. The temporal slices of the signals are achieved for $x = 0$. The insets show the numerical FF (a) and SH (b) temporal evolution in the (t, y) plane. Here the phase mismatch is $\Delta kL = 18\pi$ ($T = 142\,°C$) and the input intensity is $I = 66\ \mathrm{MW\ cm^{-2}}$.

temporal steepening effect of the trailing edge, an effect consistent with the spectra recorded experimentally (figure 8). On physical grounds, such pulse steepening is due to the asymmetrical, intensity-dependent nonlinear dragging that the walking-off SH pulse imprints on the FF pulse. Such cross-induced FF pulse steepening is made mathematically apparent, for example, by considering the higher-order corrections to the usual Kerr-like cascading limit (see [24]). In figure 10 we compare the intensities of the measured and simulated

autocorrelation traces of the FF at input and output. We stress that the autocorrelation process masks the pulse asymmetry and that the durations of the input and output pulses are approximately equal.

6. Spectral characterization

The spectral behaviours of the signals have also been analysed. We measured the spectral profiles of the pulses at the FF and the SH versus the injected intensity and at different phase
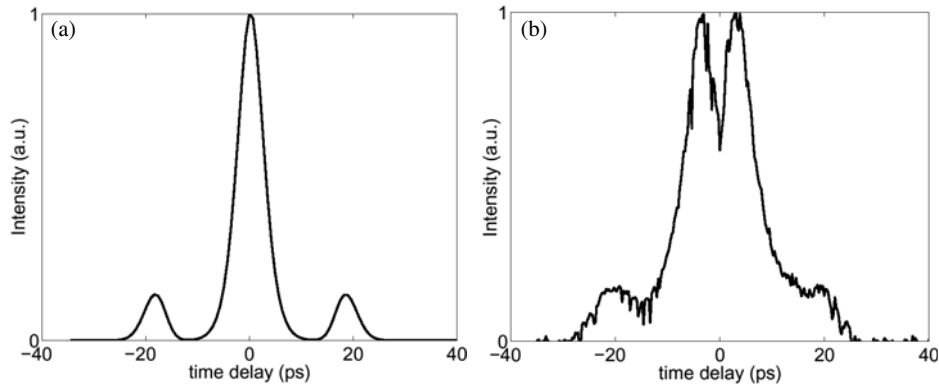
Figure 9. Spatial self-trapped regime. The cross-correlation trace in intensity of the FF and SH signals at output is shown. (a) Numerical simulation, (b) experimental data. Here the phase mismatch is $\Delta kL = 18\pi$ ($T = 142\,°C$) and the input intensity is $I = 66$ MW cm^{-2}.
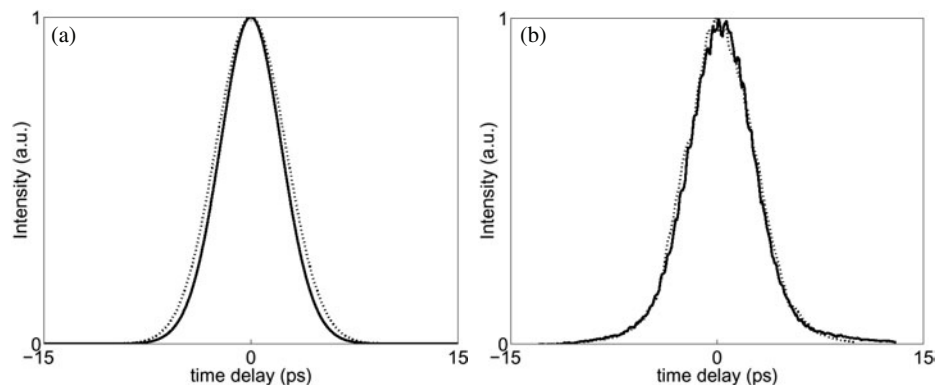

Figure 10. Spatial self-trapped regime. Autocorrelation traces in intensity of the FF at the input (dotted curve) and output (full curve) are shown. (a) Numerical simulation, (b) experimental data. Here $\Delta kL = 18\pi$ ($T = 142\,°C$) and the input intensity is $I = 66$ MW cm^{-2}.
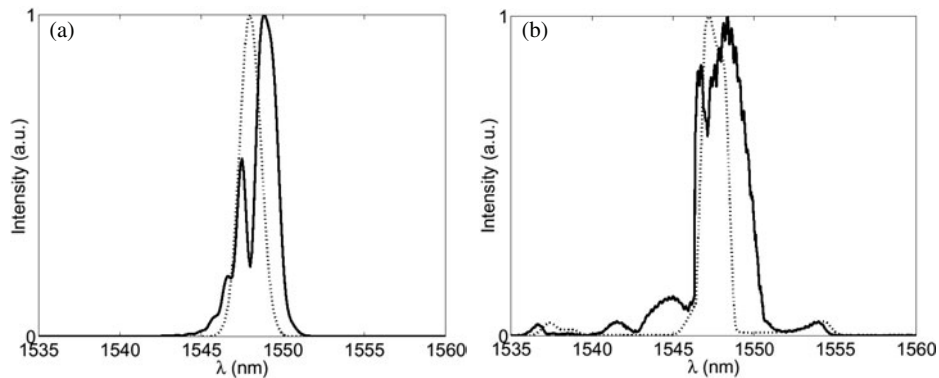

Figure 11. Spatial self-trapped regime. Pulse spectra of the FF beam at the input (dotted curve) and output (full curve). Here $\Delta kL = 18\pi$ ($T = 142\,°C$) and the input intensity is $I = 120$ MW cm^{-2}.

mismatches, focusing attention on the spatial trapping regime. The self-phase-modulation effect may involve spectral distortions; contrary to what happened in the quasi-continuous wave experiments, strong spectral changes were expected because the input pulse's spectrum can be significantly broader than the SH-generated spectral acceptance of the sample. Moreover, at high input powers, spectral broadening of the FF, which was due to self-phase modulation through cascading, was expected and clearly observed. Consequently, because of intra-spectral SH generation in the presence of the GVM, the spectra of FF and SH are modified asymmetrically, in agreement with the steepening effect discussed above. Figures 11 and 12 show typical spectral distortions of the FF and the SH after a two-fold expansion of the SH coordinates. Note the FF spectral broadening together with a wavelength shift of both the FF and SH peaks are a result of asymmetry of the phase-matching SHG condition on the wide FF spectra. Both the spectral broadening and the frequency shift of the FF and SH peaks depend consistently on the injected FF intensity and on the phase-mismatch conditions. Typical evolution of the peak spectral wavelength at the FF and the SH, versus input intensity and at a fixed positive phase mismatch, is shown in figure 13. We note a weak evolution of the peak wavelength at the FF, while at the SH a shift took place for a given intensity threshold that corresponds
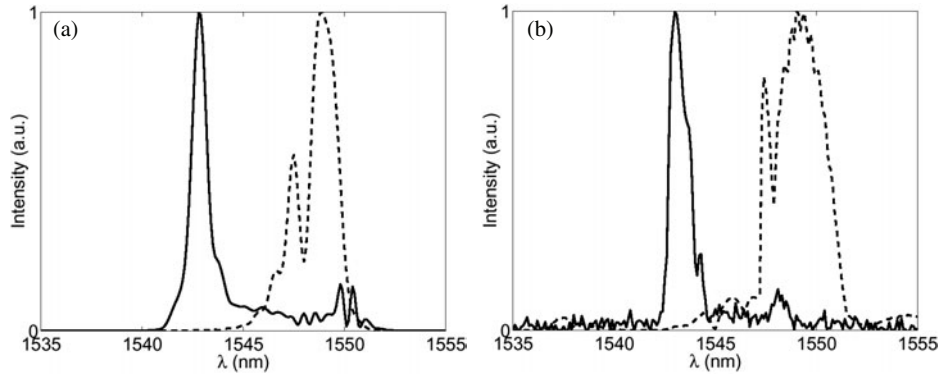
Figure 12. Spatial self-trapped regime. Output pulse spectra at the FF (broken curve) and the SH (full curve) after two-fold expansion of the SH scale. Here $\Delta kL = 18\pi$ ($T = 142\,^\circ$C) and the input intensity is $I = 120$ MW cm^{-2}.
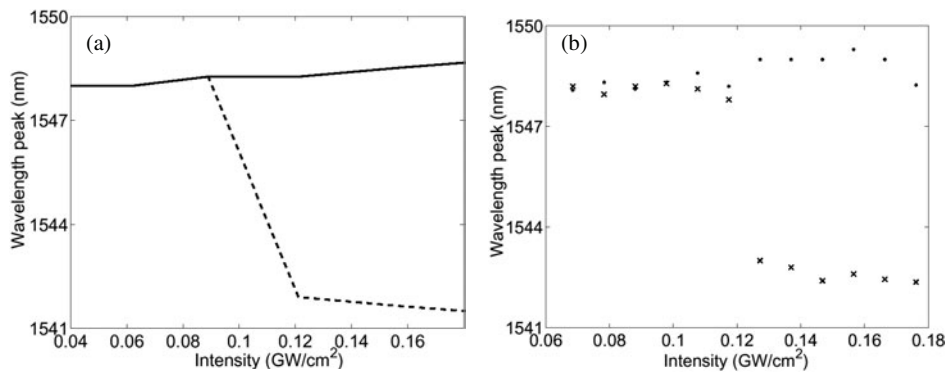

Figure 13. Peak wavelength, at the FF and the SH after a two-fold expansion of the SH scale, versus incident intensity at fixed phase mismatch (or temperature). (a) Numerical simulations: full curve, FF signal; broken curve, SH wave. (b) Experimental data: circles, FF signal; crosses, SH wave. Here $\Delta kL = 18\pi$ ($T = 142\,^\circ$C).
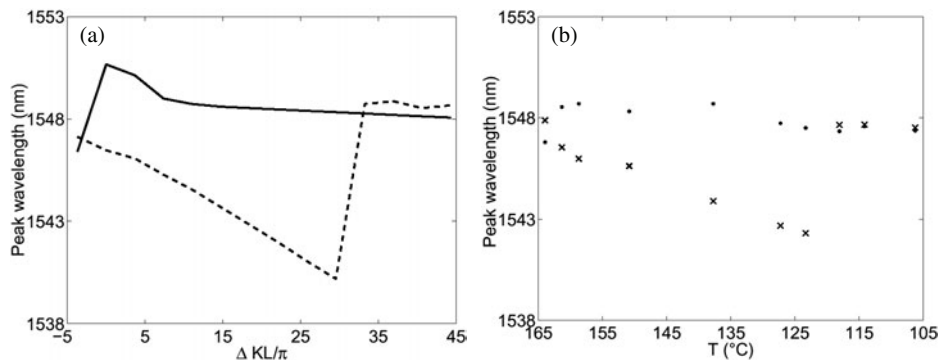

Figure 14. Peak wavelength, at the FF and the SH after a two-fold expansion of the SH scale, versus phase mismatch (or temperature) at fixed input intensity. (a) Numerical simulations: full curve, FF signal; broken curve, SH wave. (b) Experimental data: circles, FF signal; crosses, SH wave. Here $I = 140$ MW cm^{-2}.

to the spatial narrowing threshold. The typical dependence of the peak spectral wavelength versus phase mismatch, at the high intensity regime, is shown in figure 14. Notice that the peak spectral wavelength for the SH decreases almost monotonically with increasing mismatch until a threshold, which approximately coincides with the upper threshold for spatial trapping (compare with figure 4), is reached.

Finally, we notice that all the temporal spectra, and related quantities shown above correspond to the space-integrated data. Also, it is worth stressing that, in the region where spatial trapping occurs, the corresponding spatial spectra (not shown here) feature the clean shape expected from trapped beams.

7. Conclusion

We investigated numerically and experimentally the generation of spatial self-narrowed beams with 4 ps temporal pulsed excitation at 1548 nm (FF). The pump pulse duration is significantly shorter than the 20 ps temporal walk-off between interacting FF and SH waves. The experiments were performed in a film Ti:PPLN waveguide, with only the FF at input. We succeeded in exciting FF spatially self-trapped beams for a sufficiently large positive phase mismatch and above an input intensity threshold. The lowest intensity threshold measured was 45 MW cm^{-2} at a phase mismatch

$\Delta k L$ of 9π and with an input beam width of 76 μm; a linear increase of the intensity threshold on the phase mismatch was quantified. No significant temporal distortion of the FF input pulse envelope was observed during nonlinear spatial self-trapped propagation in the input intensity regime explored. A pulse steepening effect was predicted to occur on the FF signal, an effect consistent with the spectra acquired experimentally. We showed that linear temporal walk-off between the waves at FF and SH can be compensated for in the nonlinear regime. The temporal GVM compensation, and thus the temporal overlapping between the two beams, is a crucial condition for an efficient focusing cascading interaction. Broadening and slightly asymmetrical spectral modulations of the FF pulse, which are attributed to cross-induced pulse steepening, were observed together with the spatially narrowed propagation.

Acknowledgments

References

[1] Stegeman G I, Hagan D J and Torner L 1996 *Opt. Quantum Electron.* **28** 1691–740
[2] Karamzin Y N and Sukhorukov A P 1974 *JETP Lett.* **20** 339–42
[3] Stegeman G I, Sheik-Bahae M, VanStryland E W and Assanto G 1993 *Opt. Lett.* **18** 13–5
[4] Assanto G, Stegeman G I, Sheik-Bahae M and VanStryland E 1995 *IEEE J. Quantum Electron.* **31** 673–81
[5] Schiek R, Baek Y, Krijnen G, Stegeman G I, Baumann I and Sohler W 1996 *Opt. Lett.* **21** 940–2
[6] Kim S, Wang Z, Hagan D J, Van Stryland E W, Kobyakov A, Lederer F and Assanto G 1998 *IEEE J. Quantum Electron.* **34** 666–72
[7] Torruellas W E, Wang Z, Hagan D J, Van Stryland E W, Stegeman G I, Torner L and Menyuk C R 1995 *Phys. Rev. Lett.* **74** 5036–9
[8] Schiek R, Baek Y and Stegeman G 1996 *Phys. Rev.* E **53** 1138–41
[9] Di Trapani P, Caironi D, Valiulis G, Danielius R and Piskarkas A 1998 *Phys. Rev. Lett.* **81** 570–3
[10] Liu X J, Qian L and Wise F W 1999 *Phys. Rev. Lett.* **82** 4631–4
[11] Bourliaguet B, Couderc V, Barthelemy A, Ross G, Smith P R, Hanna D C and De Angelis C 1999 *Opt. Lett.* **24** 1410–2
[12] Buryak A V, Di Trapani P, Skryabin D and Trillo S 2002 *Phys. Rep.* **370** 63–235
[13] Torner L and Barthelemy A 2003 *IEEE J. Quantum Electron.* **39** 22–30
[14] Werner M J and Drummond P D 1994 *Opt. Lett.* **19** 613–5
[15] Torner L 1995 *Opt. Commun.* **114** 136–40
[16] Buryak A V and Kivshar Y S 1995 *Phys. Lett.* A **197** 407–12
[17] Peschel T, Peschel U and Lederer F 1998 *Phys. Rev.* E **57** 1127–33
[18] Carrasco S, Torner L, Torres J P, Artigas D, López-Lago E, Couderc V and Barthélémy A 2002 *IEEE J. Sel. Top. Quantum Electron.* **8** 497–505
[19] Carrasco S, Torres J P, Antigas D and Torner L 2001 *Opt. Commun.* **192** 347–55
[20] Pioger P, Couderc V, Lefort L, Barthelemy A, Baronio F, De Angelis C, Min Y, Quiring V and Sohler W 2002 *Opt. Lett.* **27** 2182–4
[21] Vassallo C 1997 *Opt. Quantum Electron.* **29** 95–114
[22] Lusse P, Stuwe P, Schule J and Unger H G 1994 *J. Light. Technol.* **12** 487–94
[23] Jundt D H 1997 *Opt. Lett.* **22** 1553–5
[24] Torres J P and Torner L 1997 *Opt. Quantum Electron.* **29** 757–76